Springer

Acta Mechanica Sinica

CrossMark click for updates

• RESEARCH PAPER •

Acta Mech. Sin., Vol. 41, 424019 (2025)
https://doi.org/10.1007/s10409-024-24019-x

Elongation enhancement strategies for AISI 430 stainless steel welded joints: insights from molecular dynamics analysis

Gongbo Bian[1], Feng Liu[2], Tingting Zhang[3,4], Mengting Ran[1], Xiaoyan Xue[1], Dinglu Wu[1], and Wenxian Wang[1*]

[1] *College of Materials Science and Engineering, Taiyuan University of Technology, Taiyuan 030024, China;*
[2] *Xi'an Seal Electronic Material Technology Co., Ltd., Xi'an 710000, China;*
[3] *College of Mechanical and Vehicle Engineering, Taiyuan University of Technology, Taiyuan 030024, China;*
[4] *Engineering Research Center of Advanced Metal Composites Forming Technology and Equipment, Ministry of Education, Taiyuan 030024, China*

Received April 24, 2024; accepted May 18, 2024; published online August 15, 2024

AISI 430 ferritic stainless steel is popular in modern industry, while conventional welding methods with filler metals produce welded joints with tensile strength (586 MPa) and elongation (7.35%), which is insufficient to meet the growing engineering requirements. In this work, the elongation of the joint is doubled (15.11%) while yield strength remains unchanged after post-weld heat treatment (PWHT). Microstructural analysis of heat affected zone (HAZ) reveals the transformation process between equiaxed ferrite, intergranular martensite, and intragranular acicular martensite in the welded joint at 750 °C and 800 °C. Additionally, molecular dynamics simulations demonstrate the impact of various types of martensite on single crystals of ferritic stainless steel under tension. The results indicate that intergranular martensite and acicular martensite demonstrate transgranular fracture, while granular martensite exhibits intragranular fracture. Intergranular martensite and granular martensite are distributed near high-strain regions within the crystal, whereas acicular martensite is concentrated at the grain boundaries, away from the high-strain regions. The comparison of hardening parameters for different types of martensite reveals that granular martensite (58.98) has higher ductility than acicular martensite (97.40) and intergranular martensite (111.54). These findings are valuable for developing advanced stainless steel welded joints that balance high ductility and strength, meeting modern engineering demands.

Welded joints, Ductility enhancement, AISI 430 ferritic stainless steel, Post-weld heat treatment, Molecular dynamics

Citation: G. Bian, F. Liu, T. Zhang, M. Ran, X. Xue, D. Wu, and W. Wang, Elongation enhancement strategies for AISI 430 stainless steel welded joints: insights from molecular dynamics analysis, Acta Mech. Sin. 41, 424019 (2025), https://doi.org/10.1007/s10409-024-24019-x

1. Introduction

AISI 430 is well-known for its commendable corrosion resistance, cost-effectiveness, and ease of fabrication. However, the increasing demand for high-performance materials underscores the necessity of enhancing AISI 430's mechanical properties, particularly in welded joints [1-3]. Traditional welding procedures can introduce complications in microstructures, potentially resulting in variations in mechanical behavior and fracture modes [4]. Industries require innovative approaches in welding technology to refine the mechanical properties of AISI 430, ensuring that it fulfills the evolving requirements of diverse applications in the field of materials engineering.

The volume fraction and morphology of the martensitic phase are the main parameters controlling the mechanical properties of stainless steel. It has been reported that increasing the volume fraction of martensite increases the strength of stainless steel but decreases its ductility [1-4]. Also the morphology of martensite is important, where martensite at ferrite grain boundaries can enhance work

*Corresponding author. E-mail address: wangwenxian@tyut.edu.cn (Wenxian Wang)
Executive Editor: Xiaoyan Li

hardening and spherical martensite can increase the strength and plasticity of steel [5-7]. Therefore it is particularly important to control the morphology and distribution of martensite in ferrite. Post-weld heat treatment (PWHT) is a process that can regulate the morphology and distribution of the microstructure within the welded joint, thereby improving its toughness [5,6]. For instance, Singh and Zafar [7] found that heat treatment at 750 °C led to M7C3→ M23C6 transformation accompanied by an increase in carbide volume fraction, Cai et al. [8] and Dong et al. [9] used PWHT to improve impact toughness (1.4 times) of martensitic heat-resistant steel and the elongation (12.7%) of friction stir welded joints of aluminum alloys. While valuable, these macroscopic properties offer limited insights into the atomistic details of microstructural changes and deformation mechanisms necessary to tailor welded joints to specific engineering requirements.

There is still a significant gap in knowledge regarding the influence of different martensite morphologies on the mechanical properties of AISI 430 welded joints. The mechanisms governing deformation and failure, especially those related to dislocation types induced by different martensite structures, are not yet fully understood. Molecular dynamics (MD) simulations have been one of the most influential tools for studying and predicting dislocation dynamics and subsequent deformation mechanisms in materials for the last two decades [10]. Many researchers have reported the mechanical properties of materials using MD simulations [11-14]. Previous research by Sun et al. [15], Ku et al. [16], and Han et al. [17] focused on the deformation behavior of ferritic stainless steel, while Zhang et al. [18], Khattak et al. [19], and Geng et al. [20] investigated the effects of welding parameters using molecular simulations. Another aspect, Shen [21] studied mechanical behavior of nano-crystalline Cu with combined grain size, strain rate and loading condition effects, Yang et al. [22] studied on micro jet in single crystal aluminum using MD, and Pogorelko and Mayer [23], Ghaffarian et al. [24], and Cui et al. [25] demonstrated the usefulness of MD simulations in understanding dislocation behavior during tensile loading, which served as inspiration for our work. While have been made commendable achievements in terms of tensile strength and elongation by focusing on macroscopic outcomes, it is necessary to have a deeper understanding of the atomistic details of microstructural changes and deformation mechanisms. The objective of this research is to investigate how different martensite morphologies influence the mechanical properties of AISI 430 welded joints, with a particular emphasis on the mechanisms that govern deformation and failure.

To address this knowledge gap, MD simulations are used to uncover atomic details of the deformation process in AISI 430 welded joints. Our goal is to examine various martensite morphologies, including intergranular, acicular, and granular, to comprehend their contributions to strengthening and toughening the ferrite matrix. This study aims to differentiate between the dislocation dynamics caused by each type of martensite during tensile loading through systematic investigations. Furthermore, we will provide a quantitative comparison of the hardening parameters associated with each type of martensite, which will allow us to rank them hierarchically based on their effectiveness in enhancing strength. Our work seeks to bridge the existing knowledge gap by exploring microstructure, dislocation behavior, and fracture modes holistically. By providing comprehensive insights to materials engineers and designers, we aim to guide the targeted design of stainless steel structures with superior mechanical properties.

2. Experimental procedure and simulation methods

2.1 Experimental procedure

The as-received base material (BM) was 4.0 mm thick plates of AISI 430 FSS (nominal composition, wt. %): Fe-0.10 C-16 Cr-0.6 Mn-0.6 Ni-0.5 Si-0.75 Mo-0.75 Cu and the filler material was ER430LNb wire of φ1.2 mm containing Fe-0.03 C-16 Cr-0.6 Mn-0.6 Ni-0.5 Si-0.75 Mo-0.75 Cu-1.2 Nb. As in Fig. 1(a) and (b), the gas metal arc welding (GMAW) process ran a welding speed of 120 mm/min under an argon shield condition with a gas flow of 15 L/min and dimensions of the samples for tensile test. The metallographic samples were etched with Marble reactant etching solutions (4 g $CuSO_4$ + 20 mL HCl + 100 mL H_2O) and microstructure was observed by optical microscope in Fig. 1 (c). The PWHT process flow diagram is shown in Fig. 1(d). The welded joints' tensile properties were tested on a material testing machine (DNS 200) at a rate of 0.02 mm/min and the fracture surface morphology was analyzed using a scanning electron microscope (SEM, JEOLJSM-6390).

2.2 Model details

The intention of the molecular simulations in this paper is to simulate the tensile process of the ferritic-martensite duplex model. All MD simulations are conducted using large atomic/molecular massively parallel simulators [26]. The atomic ferrite-martensite iron bicrystal model is shown in Fig. 2. In order to explore the influence of different types of martensite on the mechanical properties of stainless steel, the following assumptions are made in this subatomic model: (1) Since Fe and Cr are the main components in stainless steel, this model only considers Fe atoms and Cr atoms. The interaction between Fe and Cr uses the embedded-atom method (EAM) potential function provided by Eich et al. [27]; (2) The atomic model of stainless steel

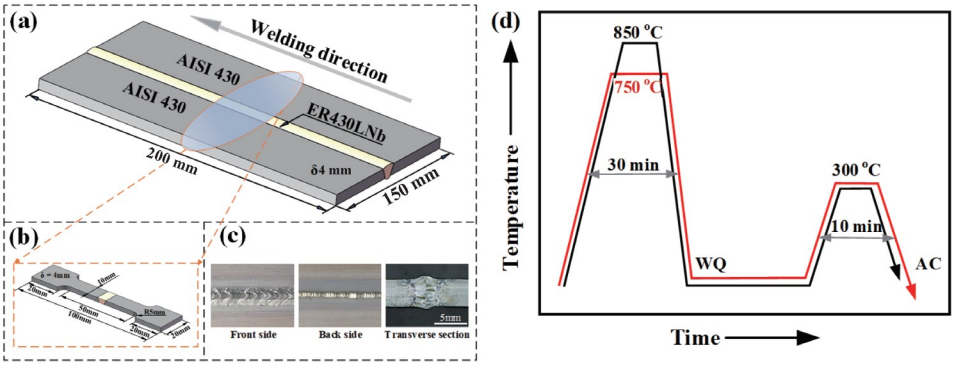

Figure 1 (a) Schematic diagram of welding process, (b) the dimensions of the samples for tensile tests, (c) macroscopic morphology and cross-section of the weld joint, (d) schematic diagram of PWHT process.

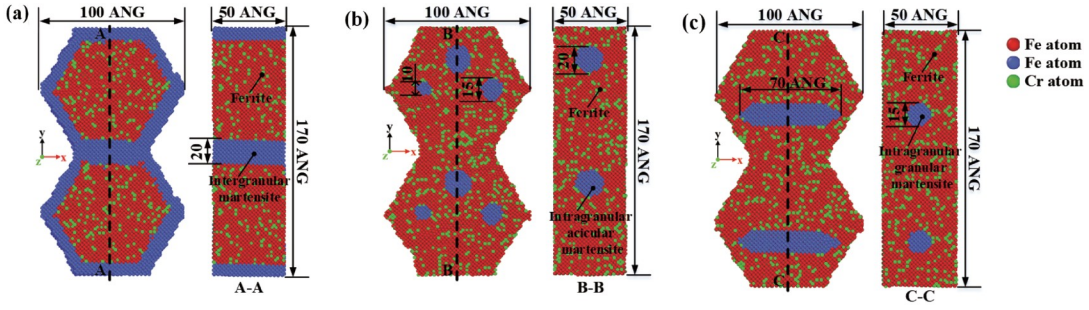

Figure 2 Atomic model diagram of ferrite-martensite iron duplex crystal structure: the dimensions of (a) ferrite with intergranular martensite (type I); (b) ferrite with intragranular granular martensite (type II); (c) ferrite with intragranular acicular martensite (type III) for tensile simulations along y direction with strain rate of 10^{10} s^{-1}. Here, Fe atoms in the ferrite phase are marked in red; Fe atoms in the martensite phase are marked in blue; Cr atoms in the ferrite phase are marked in green.

considers the two phases of martensite and ferrite, in which the atoms of martensite are all composed of Fe atoms, and the atoms of ferrite are composed of 84% Fe atoms and 16% Cr atoms. Cr atoms are inserted into the system by randomly substituting Fe atoms; (3) According to the equiaxed crystal structure characteristics of the heat-affected zone (HAZ) of the welded joint before and after heat treatment, as shown in Fig. 3(b1)-(b3), the atomic models include regular hexagonal ferrite with intergranular martensite (55808 atoms, type I), ferrite with intragranular acicular martensite (55758 atoms, type II), and ferrite with intragranular granular martensite (55666 atoms, type III). Both ferrite and martensite have a BCC structure, with corresponding lattice parameters of 2.8664 Å [28] and 2.95 Å [29], respectively. The specific dimensions of the model are shown in Fig. 2.

The effect of three different types of martensite on the tensile mechanical behavior of the ferritic-martensite duplex iron model at 300 K was studied. For each case, three independent simulations were carried out, and the results were averaged to eliminate the influence of randomness. In order to avoid the influence of free surface, periodic boundary conditions were used in all three directions.

The first step of the simulation was to relax the model. In the relaxation process, the time step was 1 fs, and the model's energy was minimized according to the conjugate gradient method. Then, the temperature of the Fe-Cr system was stable at the corresponding temperature and lasted for 100 ps according to the Nose-Hoover temperature thermostat method [30] under the NPT ensemble, and thus, the effect of model relaxation could be achieved. At this time, the pressure in the direction of the control system was kept at 1 bar.

The second step of the simulation is the tensile test, which is performed at a constant strain rate of 10^{10} s^{-1} along the *y*-direction under NVT ensemble of 300 K in order to better study the plastic deformation of metals. And the strain rate (10^{10} s^{-1}) in our MD simulations is chosen based on previous MD simulations of steels and alloys [31-34]. During the tensile process, the time step was 1 fs and the loading ended when the overall strain reached 1.

The visualization of atomic configuration is carried out using the OVITO package [35], which can use the neighbor analysis method (CNA) [36] to color the microstructure.

3. Results

3.1 Mechanical properties and fractography analysis

Figure 3(a)-(d) illustrates the fracture morphologies and tensile properties of both as-welded and post-weld heat-treated (PWHT) joints of FSS. Initially, the tensile strength

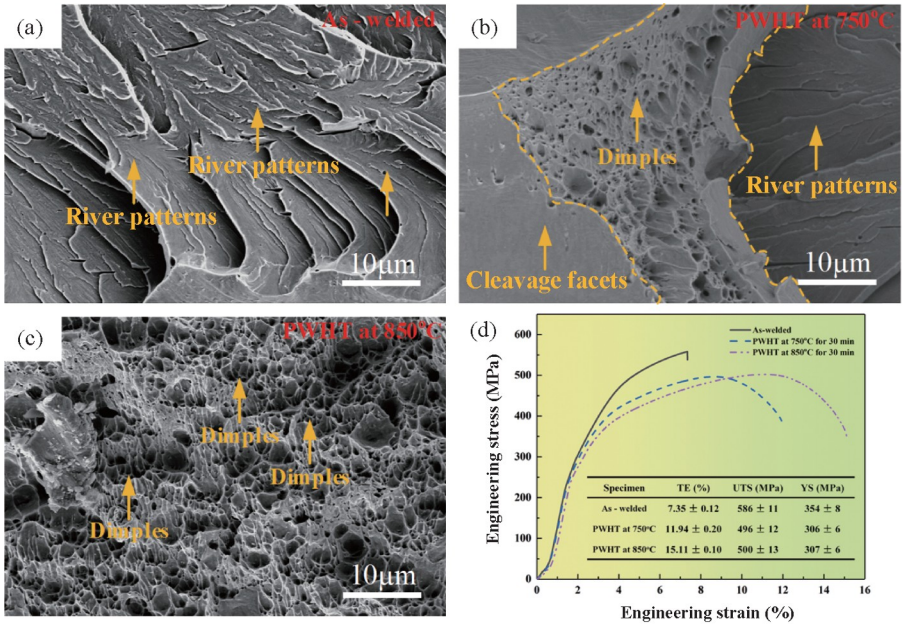

Figure 3 Fracture morphologies of (a) as-welded joints, (b) PWHT joints at 750 °C and (c) PWHT joints at 850 °C of AISI 430 FSS; (d) typical stress-strain curves.

of the welded joints is 586±11 MPa, accompanied by a tensile elongation (TE) of 7.35%. Notably, TE increases proportionally with higher PWHT temperatures. At 850 °C, PWHT yields the highest TE of 15.11%, with only a marginal decrease in tensile strength. SEM analysis is conducted to delve into the tensile fracture behavior of the welded joints. In Fig. 3(a), the as-welded joints exhibit numerous river patterns, indicative of brittle fracture. However, after PWHT, dimples emerge, with their diameter increasing as the temperature rises (Fig. 3(b) and (c)). Notably, PWHT joints at 750 °C display a combination of cleavage facets, dimples, and river patterns, suggesting a mixed tough-brittle fracture. Furthermore, PWHT joints at 850 °C exhibit larger and deeper dimples, reflecting enhanced toughness, possibly attributed to distinct microstructural features at the fracture location. This improved toughness is associated with dimples forming at the ferrite/martensite interface, where notable strength contrast and limited strain localization bands in ferrite seldom cross the interface. This phenomenon closely resembles void nucleation in dual-phase steel [37].

3.2 Microstructure and potential energy evolution

Figure 4 presents microstructure images and stress distribution across the section of both as-welded and post-weld heat-treated (PWHT) joints. Notably, the base metal and weld area exhibit minimal structural changes before and after PWHT. The base metal displays a distinct band-shaped ferrite structure elongated along the rolling direction, accompanied by M23C6 carbide particles at grain boundaries (Fig. 4(a1)-(a3)). In contrast, the weld area features coarse columnar ferrite structures (Fig. 4(c1)-(c3)).

However, the HAZ undergoes a significant transformation post-PWHT. Initially, the structure is an equiaxed ferrite with intergranular martensite (type I) at grain boundaries and intragranular acicular martensite (type III, Fig. 4(b1)). With increasing heat treatment temperature, intergranular martensite transforms into M23C6 carbide, while intragranular martensite undergoes notable changes in shape and quantity (Fig. 4(b2) and (b3)). At 750 °C, a considerable amount of granular martensite (type II) and a small amount of acicular martensite are distributed within the grain, whereas at 850°C, granular martensite primarily occupies the grain (Fig. 4(b2) and (b3)).

The changes in mechanical properties before and after heat treatment are likely correlated with the transformation of intergranular and intragranular structures in the HAZ. MD simulations were employed to explore the impact of tissue transformation on mechanical properties. The potential energy distribution analysis revealed that atomic potential energy on the grain surface is higher than within the grain, reaching up to −3.8 eV on the surface and −4.4 eV inside the grain, where atoms with the lowest potential energy are located in martensite. Additionally, atoms near martensite exhibit lower potential energy than those around ferrite, suggesting that alloy potential energy surpasses that of individual elements, as demonstrated by Ref. [38].

3.3 Molecular simulation results

3.3.1 Tensile properties of duplex crystals

MD simulation was employed to scrutinize the fracture

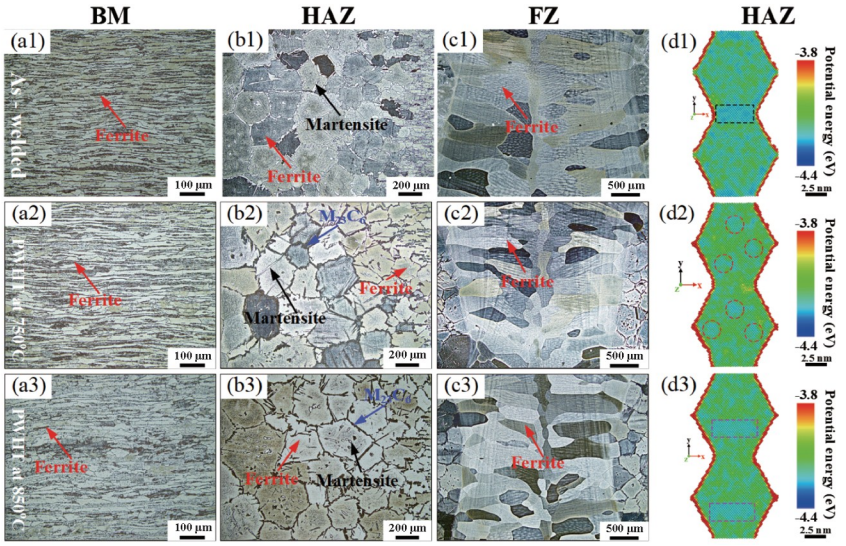

Figure 4 Microstructure images across the section of as-welded and PWHT joints: (a1, b1, and c1) as-welded, (a2, b2, and c2) PWHT at 750 °C, (a3, b3, and c3) PWHT at 850 °C; and cloud diagram of potential energy distribution at different types of microstructure: (d1) ferrite with intergranular martensite; (d2) ferrite with intragranular granular martensite; (d3) ferrite with intragranular acicular martensite.

properties of the ferrite/martensite interface in duplex crystals. The results of the simulation, utilizing ferrite in conjunction with three types of martensite, are detailed herein. Figure 5(a) depicts the matrix post-relaxation at 300 K, presenting the radial distribution function diagram of Fe atoms in ferrite and martensite. The peaks at approximately 2.48, 2.85, 4.1, and 4.75 Å signify the typical body-centered cubic (BCC) crystal structure at 300 K [39]. Figure 5(c) shows the crystal structure information of the soldered and PWHT joints. The results show that ferrite and martensite phases are mainly present in the matrix of stainless steel before and after heat treatment, which is in agreement with the previous work [40,41]. Meanwhile, the corresponding high diffractive indexes of ferrite are (110) and (200), while the corresponding high diffractive index of martensite is (211). In addition, the lattice parameters of ferrite-martensite are calculated to be 2.86 and 2.97 Å, respectively, which are consistent with the RDF distributions calculated in this simulation (as shown in Fig. 5(a)). Remarkably, the interaction between Fe atoms in martensite, as indicated by the main peak in the radial distribution function, is significantly stronger than that in ferrite. This heightened interaction results in vigorous motion among Fe atoms in martensite, converting more potential energy into kinetic energy. This phenomenon aligns with the potential energy distribution of different martensite forms (Fig. 4(d1)-(d3)). Tensile stress, computed using the virial stress expression [42], and engineering strain, calculated by comparing boundary distances in the *y*-direction of the MD model, are illustrated in Fig. 5(b). The stress-strain curve reveals distinct stages: a brief elastic stage, followed by peak tensile stress; subsequent internal damage leading to a plastic stage; rapid crack propagation causing a sharp decrease in tensile stress; and eventual rupture of the two-phase model. During the tensile process, the plastic stage is defined by the dislocation line, when the material enters the plastic deformation stage, dislocation lines begin to appear and change with the increase of strain, and when the dislocation lines disappear, the material enters the fracture stage [10,21]. Combined with the dislocation evolution

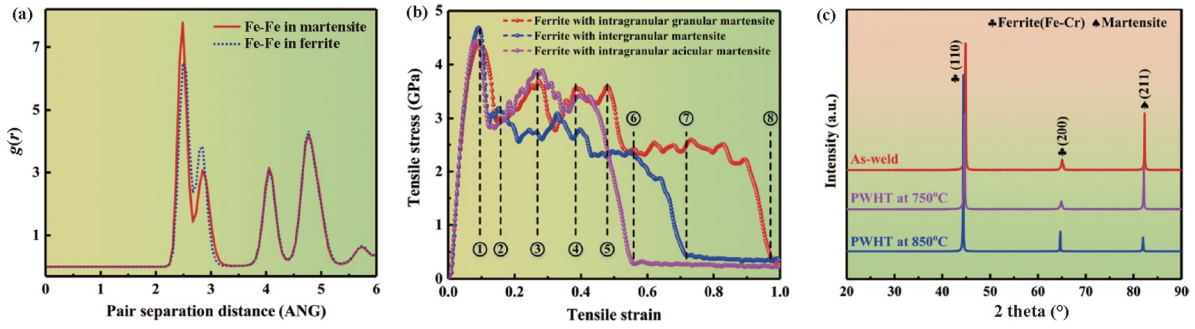

Figure 5 (a) Radial distribution function (RDF) curves of Fe-Fe atoms in ferrite and martensite after relaxation at 300 K; (b) tensile tests of ferrite with three types of martensite at 300 K; (c) XRD patterns of as-welded and PWHT joints.

diagrams (as described in Sect. 3.3.4), key points and stages in this process are marked in Fig. 5(b): maximum stress point (①), first reduction point of tensile stress (②), plastic stages (from ② to ⑤), breaking point of the type III duplex model (⑥), breaking point of the type I duplex model (⑦), and breaking point of the type II duplex model (⑧). Furthermore, the tensile curve results reveal maximum tensile stresses of approximately 4.42, 4.68, and 4.44 GPa for the three duplex crystals, with corresponding stress ranges in the plastic stage and maximum fracture strains summarized in Table 1. Herein, stress fluctuation is the range of variation of tensile stress during the plastic deformation stage for each tensile case, i.e., from the minimum to the maximum value of tensile stress, according to Fig. 5(b).

3.3.2 Structural evolution of ferrite-martensite iron duplex crystals

Figure 6 illustrates the eight distinctive atomic arrangements of various two-phase crystal models throughout the stretching process, corresponding to points marked as ①-⑧ on the stretching curve (Fig. 5(b)). Twin crystal models of different martensite types exhibit localized deformations influenced by tensile loading. Intragranular martensite experiences more pronounced atomic deformation fluctuations than intergranular martensite during the tensile process. During the elastic stage (elastic strain < 0.132), atoms in all phases largely maintain their integrity, with only slight deformations observed in type I and type III martensite (Fig. 6-① and ②). Beyond an elastic strain of 0.28, irreversible position changes in martensite and ferrite atoms indicate plastic deformation (Fig. 6-③ and ④). At a strain of 0.426, dual-phase crystals undergo noticeable elongation in the tensile direction, signifying the initiation of necking down (Fig. 6-⑤).

Remarkably, fractures in different types of martensite result in distinct strains and fracture positions. Type I martensite fractures at a strain of 0.72, with the fracture occurring in intergranular martensite, while the ferrite undergoes severe deformation without breaking (Fig. 6(a)-⑦), aligning with the breaking point of the tensile curve (Fig. 5-⑦). Type III martensite fractures at a strain of 0.564, with the fracture location at the grain boundary line (Fig. 6(c)-⑤), consistent with the tensile curve's fracture point (Fig. 5-⑥). Type II martensite fractures at a strain of 0.99, and the fracture occurs inside the ferrite (Fig. 6(b)-⑧), consistent with the tensile curve's fracture point (Fig. 5-⑧). This underscores the relationship between the strength of the PWHT welded joint and the content of type I and type III martensite, while the fracture strain correlates with the content and distribution of type II martensite.

Figure 7 provides a detailed analysis of the microstructural evolution of the dual-phase crystal under varying strains. Before reaching maximum stress, each atom exhibits movement around its equilibrium point, maintaining an or-

Table 1 Tensile tests results for the duplex iron crystal model

Duplex atomic model	Maximum tensile stress (GPa)	Stress fluctuation in plastic stage (GPa)	Maximum fracture strain
Intergranular martensite / Ferrite (I)	4.68	2.55-3.00	0.72
Intragranular granular martensite / Ferrite (II)	4.44	2.77-3.59	0.99
Intragranular acicular martensite / Ferrite (III)	4.42	2.81-3.88	0.56

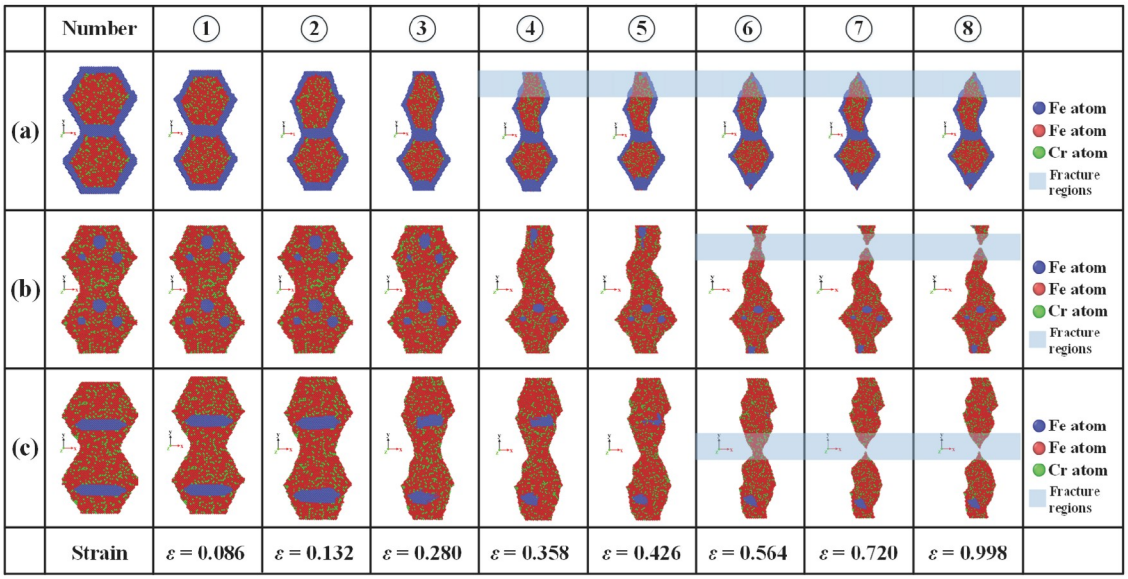

Figure 6 Evolution diagram of representative atomic configuration throughout the tensile process under different strains of: (a) ferrite with intergranular martensite; (b) ferrite with intragranular granular martensite; (c) ferrite with intragranular acicular martensite at 300 K. Here, Fe atoms in the ferrite phase are marked in red; Fe atoms in the martensite phase are marked in blue; Cr atoms in the ferrite phase are marked in green.

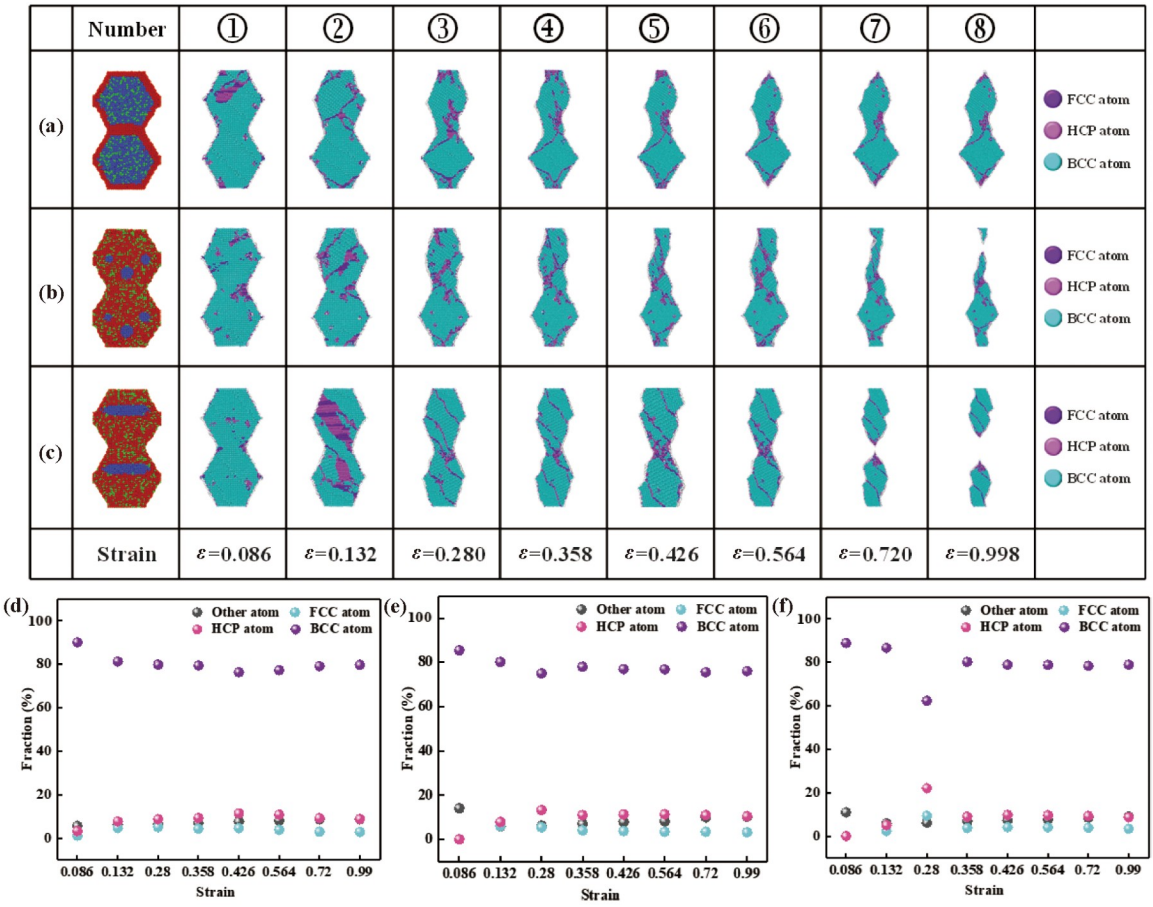

Figure 7 Structural type evolution diagram and histogram of structural type proportions under different strains during tensile tests of ferrite with: (a) and (d) intergranular martensite; (b) and (e) intragranular granular martensite; (c) and (f) intragranular acicular martensite at 300 K. Here, HCP-type atoms are marked in pink; BCC-type atoms are marked in purple; FCC-type atoms are marked in cyan; besides, other atoms are marked in white.

dered BCC-type arrangement in the twin-crystal atomic model. As strain increases, reaching 0.132, some atoms within the matrix convert into hexagonal close-packed (HCP) and face-centered cubic (FCC)-type dislocation atoms due to the elevated system energy.

After attaining of maximum tensile stress, stacking fault nucleation becomes evident near the martensite-ferrite interface. FCC and HCP atoms rapidly expand toward the stacking faults, with a more pronounced effect observed at the interface between type III martensite and ferrite (Fig. 7 (c)-②). Continuing the tensile process, strain incrementally rises, causing the transformation of FCC and HCP atoms on stacking faults into other atom types. The stacking faults move away from the martensite-ferrite interface, expanding and aggregating toward crack defects (Fig. 7-③, ④, and ⑤), indicating the material's entry into the plastic stage.

At a strain of 0.564, stacking faults at cracks further intensify, primarily comprising HCP-type faults. Simultaneously, the necking down of the material commences (Fig. 7-⑥ and ⑦). When cracks appear, atoms inside the crystal revert to movement around their equilibrium position, maintaining the ordered BCC lattice type. During the fracture stage, the distribution positions of HCP-type atoms vary among different crystals. Type I and type III martensite predominantly exhibit HCP-type atoms at the fracture position, while type II martensite features an internal distribution of HCP-type atoms (Fig. 7-⑧). This highlights the potential influence of different martensite types on the mechanical properties of the crystal, particularly tensile elongation, by affecting the distribution of HCP-type atoms during material fracture. Furthermore, Fig. 7(d)-(f) illustrate the crystal's evolution process of atomic type proportions under different strains.

3.3.3 Stress-strain analysis of duplex crystal models during tensile deformation

Stress contour plots help predict the crack propagation trend at the ferrite/martensite interface of crystals during the tensile process [43]. The six stress components are monitored during the crack propagation process. Although the von Mises stress originates from the metal yield criterion on the macro scale, it also applies to the nanoscale [44]. In terms of normal and shear stress, the von Mises stress is given by

$$\sigma_{\text{von}} = \left\{\frac{1}{2}\left[(\sigma_{xx}-\sigma_{yy})^2+(\sigma_{xx}-\sigma_{zz})^2+(\sigma_{zz}-\sigma_{yy})^2\right] +3\left(\sigma_{xy}^2+\sigma_{yz}^2+\sigma_{xz}^2\right)\right\}^{\frac{1}{2}}, \quad (1)$$

where σ_{ij} is the components of the virial stress tensor; the subscript i and j are the cartesian components.

Figures 8 and 9 present the von Mises stress distribution and plastic strain distribution diagrams of atoms in crystals of different martensite types during the tensile process, corresponding to the detailed simulation in Fig. 5 (marked as ①-⑧). Before reaching the maximum tensile stress, indicative of the elastic stage, the crystal undergoes minimal elastic deformation, with a notable high Mises stress value reaching approximately 15 GPa (Fig. 8-①). At a strain of 0.132, intragranular martensite exhibits larger high-stress areas than intergranular martensite (Fig. 8-②), and the crystal experiences almost no deformation (Fig. 9-① and ②). Notably, some matrix atoms transform into HCP and FCC-type stacking faults (Fig. 7-②), suggesting that this transformation during the elastic stage is driven by local high stress rather than strain.

As tensile strain increases, the crystal transitions to the plastic stage, featuring a relatively high-stress field at the stacking fault (Fig. 8-③, ④, and ⑤). Simultaneously, plastic deformation accumulates, causing damage inside the crystal, with some atoms exhibiting higher plastic strains

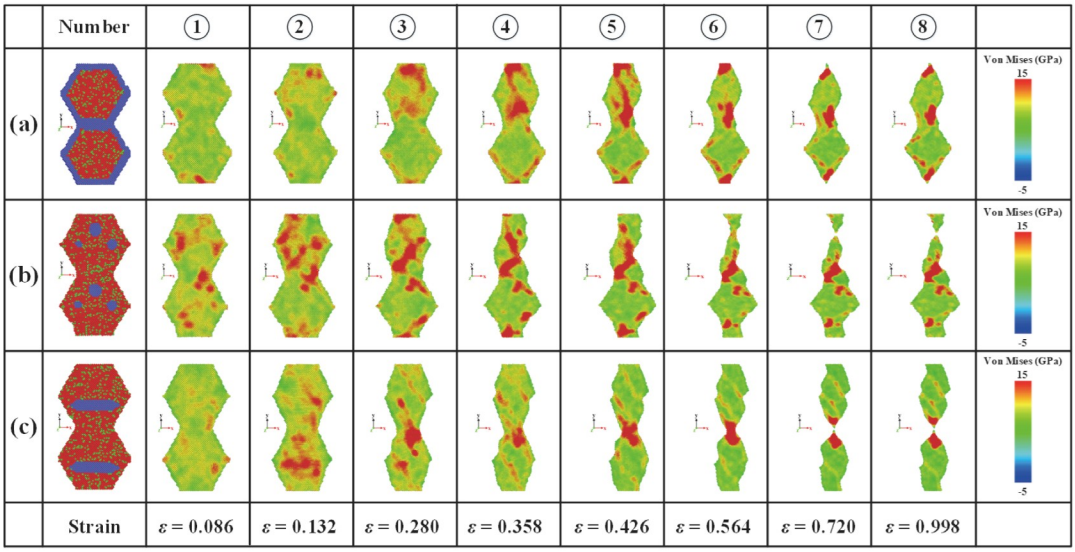

Figure 8 Von Mises stress distribution cloud diagram under different strains of ferrite with: (a) intergranular martensite; (b) intragranular granular martensite; (c) intragranular acicular martensite at 300 K. Here, Fe atoms in the ferrite phase are marked in red; Fe atoms in the martensite phase are marked in blue; Cr atoms in the ferrite phase are marked in green.

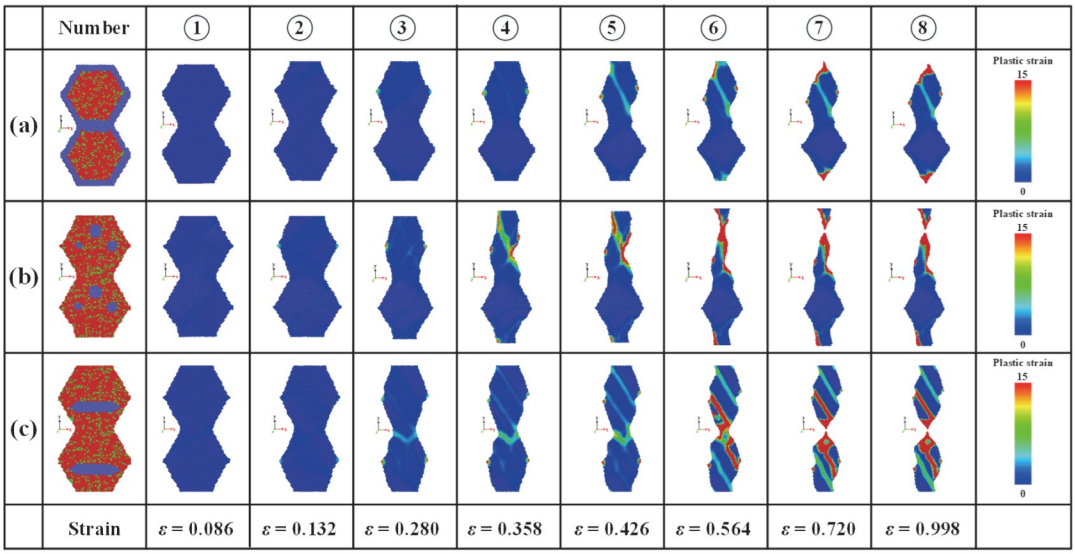

Figure 9 Plastic strain distribution cloud diagram during tensile tests of ferrite with: (a) intergranular martensite; (b) intragranular granular martensite; (c) intragranular acicular martensite at 300 K. Here, Fe atoms in the ferrite phase are marked in red; Fe atoms in the martensite phase are marked in blue; Cr atoms in the ferrite phase are marked in green.

(Fig. 9-③, ④, and ⑤). The direction of plastic deformation is at a 45° angle to the stretching direction. Uneven local plastic deformation within the grain leads to an uneven stress field distribution. For type I and type II martensite, the high-stress area is mainly distributed inside the crystal near the high-stress area of martensite. For type III martensite, the high-stress region concentrates at grain boundaries, distant from the high-strain region of martensite (Fig. 9-⑤). This suggests that under a high-strain field, type III martensite causes concentrated high stress at grain boundaries, intensifying damage and leading to premature crack expansion.

During the fracture stage of the crystal, notable high-stress fields (Fig. 8-⑥, ⑦, and ⑧) and extensive plastic strain fields (Fig. 9-⑥, ⑦, and ⑧) are observed at HCP-type atoms within the crystal. Different martensite types exhibit variations in the distribution of crystal stress fields and plastic deformation. In the case of a type I martensite crystal fracture, high stress is concentrated in the martensite atoms at the fracture end, resulting in an intergranular break. Martensite atoms at both ends experience significant stress, while the middle region undergoes minimal plastic deformation. Conversely, when a type II martensite crystal fractures, the high-stress area is distant from the fracture position, occurring inside the ferrite and manifesting as a transgranular fracture. The fracture position exhibits substantial plastic strain, indicating significant damage in this region. Type III martensite crystals showcase high stress at the fracture location, which occurs at the grain boundary between ferrites, representing an intergranular fracture. Simultaneously, during crystal fracture, a substantial gap emerges between the fracture location and the intragranular structure, accompanied by plastic deformation. The deformation direction and the tensile direction form an angle of 45°.

In summary, type I and type III martensite crystals predominantly fracture at grain boundaries, displaying an intergranular fracture pattern, potentially rendering ferritic stainless steel more prone to brittleness upon fracture. In contrast, type II martensite crystals primarily fracture within the ferrite crystal, adopting a transgranular fracture pattern that imparts toughness to ferritic stainless steel during fracture.

3.3.4 Dislocation analysis during tension of duplex crystals

Dislocation and defect analysis (slip system determination) was carried out with the help of the dislocation extraction algorithm (DXA) developed by Stukowski and Albe [45]. Figure 10 illustrates the internal dynamic dislocation evolution of different martensite/ferrite dual-phase crystals

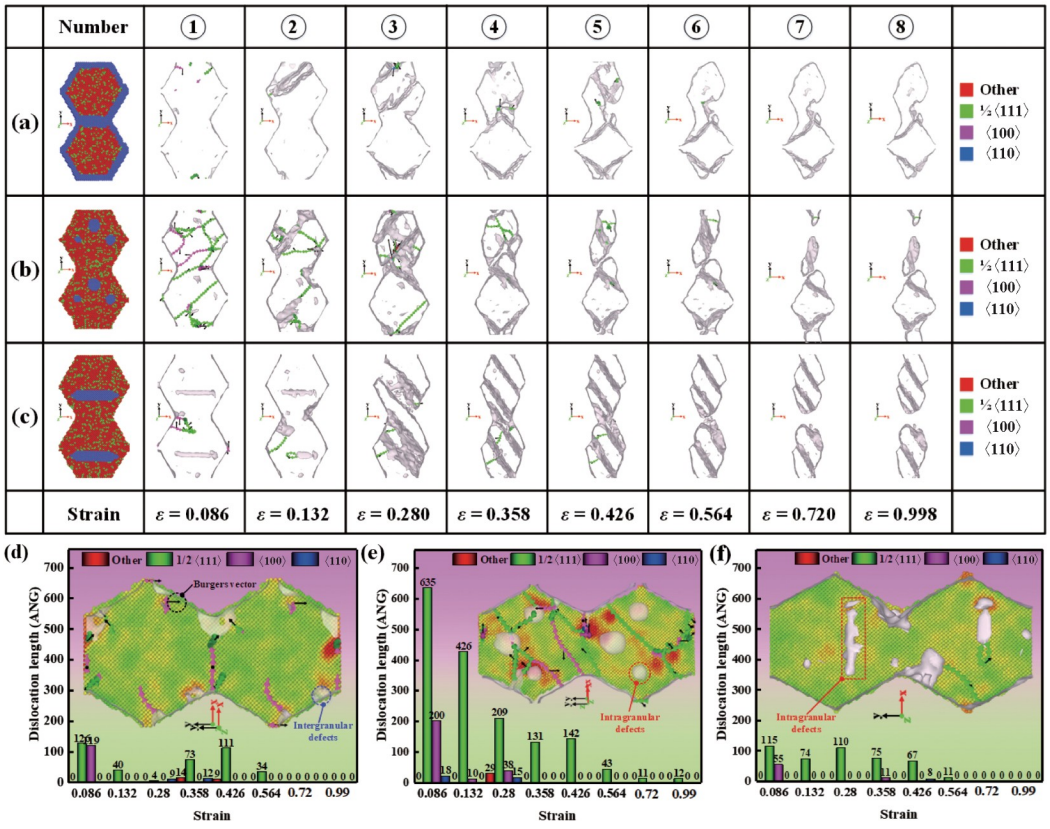

Figure 10 Dislocation evolution diagram and histogram of dislocation length under different strains during tensile process of ferrite with: (a) and (d) intergranular martensite; (b) and (e) intragranular granular martensite; (c) and (f) intragranular acicular martensite at 300 K. Here, Fe atoms in the ferrite phase and other dislocations are marked in red; Fe atoms in the martensite phase and ⟨110⟩ dislocations are marked in blue; Cr atoms in the ferrite phase and 1/2⟨111⟩ dislocations are marked in green; ⟨100⟩ dislocations marked in pink.

during the tensile process, corresponding to key moments on the tensile curve in Fig. 5 (refer to marked points ①-⑧). The deformation process is primarily characterized by 1/2⟨111⟩ and ⟨100⟩ dislocations, with four main types observed: 1/2⟨111⟩, ⟨100⟩, ⟨110⟩, and other dislocations. The propagation and annihilation of these dislocations contribute to the plastic deformation mechanism.

At a strain of 0.086 (Fig. 10(a)-(c)), dislocations emerge in all dual-phase crystals, predominantly 1/2⟨111⟩ and ⟨100⟩ (Fig. ①). At a strain of 0.132, corresponding to the first peak in tensile stress, dislocation lines, mainly 1/2⟨111⟩, reach a high total length (Fig. ②). This signifies the highest tensile stress in the elastic phase due to dislocation generation and evolution. As the material transitions to the plastic stage, dislocation length remains relatively constant. Internal damage occurs at a strain of 0.426 primarily near stacking fault atoms. For type I and type III martensite, 1/2⟨111⟩ dislocations are mainly in the ferrite matrix, while for type II martensite, 1/2⟨111⟩ dislocations are not only in the ferrite matrix but also nucleate around stacking faults (Figs. ③, ④, and ⑤). As the tensile process progresses, the material experiences fracture behavior, leading to the disappearance of dislocation lines inside the crystal (Figs. ⑥, ⑦, and ⑧).

Figure 10(d)-(f) present statistical diagrams of dislocation line lengths for different types of martensite dual-phase crystals during the tensile process. In type I martensite, 1/2⟨111⟩ and ⟨100⟩ mixed dislocations dominate, with dislocation line length initially increasing and then decreasing, disappearing after fracture. Type I martensite acts as discontinuous block defects concentrated at grain boundaries during tensile stress (Fig. 10(d)). For type II martensite, 1/2⟨111⟩ mixed dislocations prevail, with dislocation line length decreasing with strain but persisting post-fracture. Spherical defects are distributed in high-stress areas within the grain during the tensile process (Fig. 10(e)). Type III martensite exhibits mainly 1/2⟨111⟩ mixed dislocations, with unchanged dislocation line length before and after fracture. It acts as extended strip defects concentrated in intragranular stress areas during the tensile process (Fig. 10(f)).

4. Discussion

4.1 The relationship between mechanical properties and dislocation density

In order to analyze the relationship between the dislocation density and mechanical properties within the crystal during the tensile process, the static yield strength is determined by the Taylor hardening law [46,47], which is used to describe the relationship between the material yield strength and dislocation density:

$$Y = \alpha G b_D \sqrt{\rho_D}, \tag{2}$$

where α is the hardening parameter. The static yield strength Y is the bottom limit, which can be reached only at very slow deformation. G is the shear modulus. b_D and ρ_D are the modulus of the Burgers vector of moving dislocations and the dislocation density, respectively. In addition, the value of b_D is 2.5×10^{-10} m, and the dislocation density is calculated indirectly, and its calculation formula is

$$\rho_D = \frac{l}{V}, \tag{3}$$

where ρ_D is the dislocation density, l is the total dislocation length, and V is the volume of the deformed crystal. Herein, V takes a value of about 650 nm^3, and it is assumed that the crystal volume remains constant during tension.

The simulation results reveal that through linear fitting using Eq. (2), the static yield strength of the material exhibits a linear correlation with the 1/2 power of the dislocation density for various martensite types. The fitting degree, R^2, is approximately 0.9. The hardening parameter α values follow the order: 111.54 (intergranular martensite) > 97.40 (acicular martensite) > 58.98 (granular martensite). A higher hardening parameter suggests a greater inclination towards brittle fracture. This implies that intergranular and acicular martensite may induce brittle fracture in ferritic stainless steel, while granular martensite may lead to plastic fracture. Moreover, in the case of intergranular and acicular martensite, material fracture occurs between the grains, which is indicative of an intergranular fracture. In contrast, for granular martensite, the fracture position is within the ferrite, representing a typical through-grain crystal fracture (Fig. 11). Figure 11(d) depicts the correlation between the hardening parameter and tensile elongation during deformation. The figure clearly shows that the hardening parameter of the material shows a tendency to decrease and then increase as the martensite transforms from type I to type III, however, the elongation shows a tendency to increase and then decrease. This is due to the fact that the deformation behavior of the material is not only related to the shape but also to the distribution of the martensite. Type I is prone to cracking due to the presence of high hardening parameters as it is located at the grain boundaries (Fig. 11(a)), but the internal ferrite matrix is in continuous distribution during the deformation process, which leads to the good plasticity of the type I martensite. At the same time, type III martensite has poor plasticity due to its distribution inside the matrix and its needle-like shape (Fig. 11(c)), which interrupts the continuous distribution of the ferrite matrix, thus making type III martensite have poor plasticity.

4.2 Mechanism of strengthening and toughening of martensite in stainless steel

In order to comprehend the mechanical behavior of ferritic

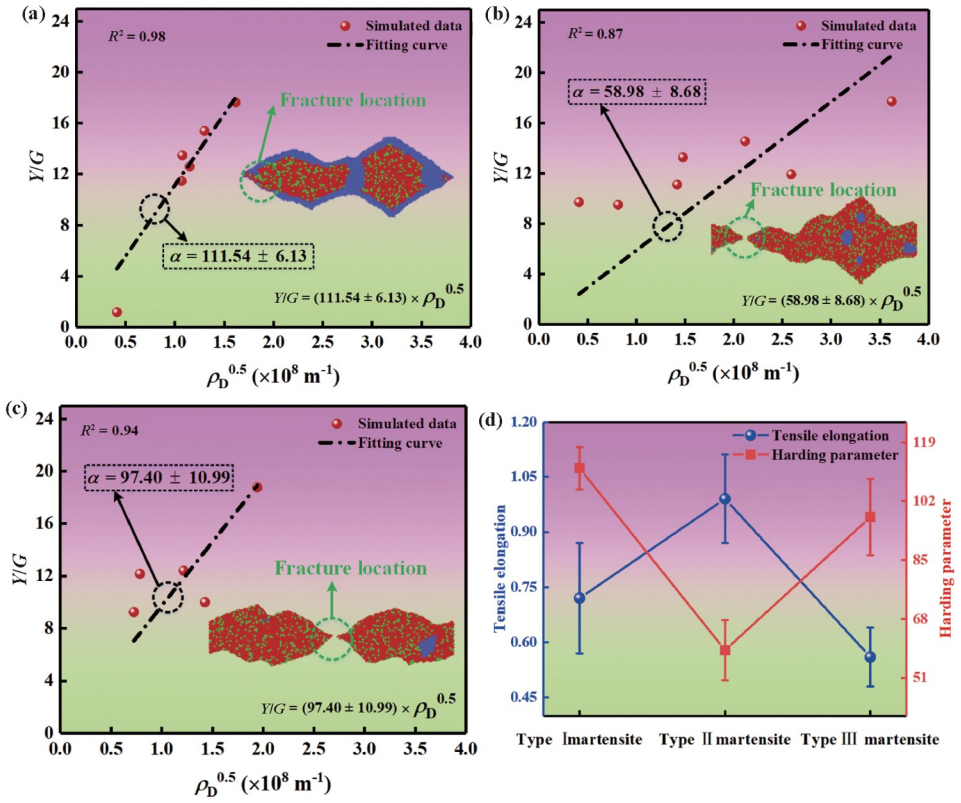

Figure 11 Correlation diagram between yield strength and dislocation density of ferrite with: (a) intergranular martensite; (b) intragranular granular martensite; (c) intragranular acicular martensite at 300 K; (d) the relationships between hardening parameter and tensile elongation.

stainless steel welded joints, a relationship diagram correlating mechanical properties with microstructure was constructed (Fig. 12). Notably, an increase in PWHT temperature results in a gradual reduction in the tensile strength of the welded joint, while the elongation after fracture exhibits a corresponding gradual increase.

MD findings elucidate that intergranular martensite and acicular martensite induce a significant presence of HCP-type stacking faults in the grain. Simultaneously, a high hardening parameter α is observed, with dislocation types characterized as 1/2⟨111⟩ mixed dislocations, leading to intergranular fracture—a common precursor to material brittleness. Conversely, granular martensite exhibits a higher dislocation density, a lower hardening parameter α, and a transgranular fracture mode, indicative of ductile fracture behavior during the tensile process.

Within the welded HAZ, a predominant distribution of intergranular martensite, acicular martensite, and ferrite is noted. Subsequent deformation processes lead to a substantial presence of HCP-type stacking faults, resulting in a high hardening parameter that imparts elevated strength but reduced plasticity to the ferritic stainless steel. Following PWHT at 750 °C, the HAZ primarily comprises granular martensite, ferrite, and intergranular martensite transformed M23C6. The deformation process involves FCC and HCP-type stacking faults, yielding a microstructure with similar

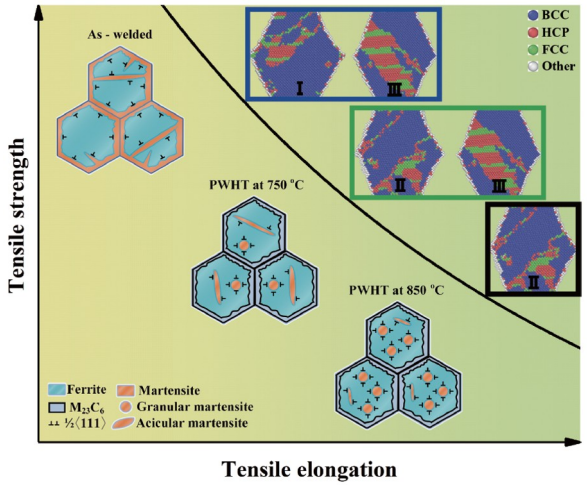

Figure 12 Schematic diagram of the strengthening and toughening mechanism of ferritic stainless steel.

morphology and relatively uniform distribution, ultimately rendering the ferritic stainless steel highly tough. The sphericization of martensite achieved through PWHT at 850 °C serves a dual purpose: it eliminates local stress concentration [48]. It enables continuous spatial deformation of ferrite due to the discrete distribution of martensite [49]. This culminates in the highest toughness for the ferritic stainless steel.

5. Conclusions

In conclusion, this study presents a comprehensive investigation into the fabrication and MD analysis of welded joints made from AISI 430 ferritic stainless steel, mainly focusing on the effects of PWHT. The welded joints, after PWHT, exhibited notable mechanical properties, with an ultimate tensile strength of 500 MPa and an elongation of 15%, highlighting the impact of thermal treatment on enhancing ductility.

The study deciphers the intricate interactions between different types of martensite and the ferrite matrix during the deformation process through MD simulations. The findings underscore distinct mechanisms for strengthening and toughening effects. Intergranular and acicular martensite induced a substantial presence of hexagonal close-packed (HCP) dislocations within the grain, featuring a $1/2\langle 111\rangle$ mixed dislocation. Simultaneously, intergranular martensite manifested a brittle fracture mode with intergranular fracture, while granular martensite exhibited a ductile transgranular fracture mode. Hardening parameters ranked intergranular martensite highest, followed by acicular and granular martensite.

This research significantly contributes to the field by providing insights essential for designing high ductility and high-strength stainless steel welded joints. The consideration of PWHT effects further emphasizes the practical applicability of the study, offering a roadmap for optimizing welding processes and materials in engineering applications.

Conflict of interest *On behalf of all authors, the corresponding author states that there is no conflict of interest.*

Author contributions ***Gongbo Bian:*** *Conceptualization, Methodology, Investigation, Writing – original draft, Visualization.* ***Feng Liu:*** *Investigation, Funding acquisition, Supervision.* ***Tingting Zhang:*** *Writing – review & editing.* ***Mengting Ran:*** *Writing – review & editing.* ***Xiaoyan Xue:*** *Investigation, Conceptualization.* ***Dinglu Wu:*** *Writing – review & editing.* ***Wenxian Wang:*** *Supervision, Project administration, Funding acquisition.*

Acknowledgements *This work was supported by the National Natural Science Foundation of China (Grant Nos. 52075360, 52275360, and 51805359).*

1 J. Cui, Z. Yao, F. Cheng, Y. Cui, G. Wang, L. Wang, H. Sun, S. Li, Z. Wen, and J. Sun, Corrosion resistance of a tungsten modified AISI 430 stainless steel bipolar plate for proton exchange membrane fuel cells, RSC Adv. **6**, 31367 (2016).
2 J. S. Peltz, L. M. Antonini, S. R. Kunst, G. A. Ludwig, L. T. Fuhr, and C. F. Malfatti, Effect of application of the shot peening process in the corrosion resistance of the AISI 430 ferritic stainless steel, Mater. Sci. Forum **775-776**, 365 (2014).
3 S. K. Yen, and Y. C. Tsai, Determination of the critical temperature for forming a chromium-rich oxide on AISI 430 stainless steel and its corrosion resistance, J. Electrochem. Soc. **143**, 2493 (1996).
4 U. Zerbst, R. A. Ainsworth, H. T. Beier, H. Pisarski, Z. L. Zhang, K. Nikbin, T. Nitschke-Pagel, S. Münstermann, P. Kucharczyk, and D. Klingbeil, Review on fracture and crack propagation in weldments—A fracture mechanics perspective, Eng. Fract. Mech. **132**, 200 (2014).
5 C. Köse, Heat treatment and heat input effects on the dissimilar laser beam welded AISI 904L super austenitic stainless steel to AISI 317L austenitic stainless steel: Surface, texture, microstructure and mechanical properties, Vacuum **205**, 111440 (2022).
6 W. Jia, H. Zhao, Y. Zan, P. Guo, and X. Mao, Effect of heat treatment and laser shock peening on the microstructures and properties of electron beam welded Ti-6.5Al-1Mo-1V-2Zr joints, Vacuum **155**, 496 (2018).
7 B. Singh, and S. Zafar, Influence of post clad heat treatment on microstructure and slurry erosion characteristics of Ni-based microwave clad, Vacuum **184**, 109946 (2021).
8 H. Cai, L. Xu, L. Zhao, and Y. Han, Application of post-weld treatment (PWHT) in improving properties of martensitic heat-resistant steel thick plate by cold metal transfer plus pulse (CMT + P) welding, J. Mater. Sci. **57**, 21552 (2022).
9 J. Dong, D. Zhang, W. Zhang, G. Cao, and C. Qiu, Effect of post-weld heat treatments on the microstructure and mechanical properties of underwater friction stir welded joints of 7003-T4/6060-T4 aluminium alloys, Mater. Sci. Eng.-A **862**, 144423 (2023).
10 M. Wang, F. Wang, J. Zhang, H. Wang, Y. Wang, and H. Wu, Effects of h-BN additives on tensile mechanical behavior of Fe matrix: A molecular dynamics study, Comput. Mater. Sci. **223**, 112136 (2023).
11 W. Xia, L. Li, Y. Wei, A. Zhao, Y. Guo, C. Huang, H. Yin, and L. Zhang, Impact toughness of a gradient hardened layer of Cr5Mo1V steel treated by laser shock peening, Acta Mech. Sin. **32**, 301 (2016).
12 Z. L. Liu, Z. Zhuang, X. M. Liu, X. C. Zhao, and Y. Gao, Bauschinger and size effects in thin-film plasticity due to defect-energy of geometrical necessary dislocations, Acta Mech. Sin. **27**, 266 (2011).
13 B. N. Legarth, Necking of anisotropic micro-films with strain-gradient effects, Acta Mech. Sin. **24**, 557 (2008).
14 Z. Duan, X. F. Ma, H. J. Shi, R. Murai, and E. Yanagisawa, Gigacycle fatigue behaviors of two SNCM439 steels with different tensile strengths, Acta Mech. Sin. **27**, 778 (2011).
15 J. Sun, H. Tang, C. Wang, Z. Han, and S. Li, Effects of alloying elements and microstructure on stainless steel corrosion: A review, Steel Res. Int. **93**, 2100450 (2022).
16 M. H. Ku, G. J. Shu, Y. J. Tsai, Y. K. Huang, S. X. Chi, Y. C. Wen, and M. W. Wu, The effects of microstructures on the mechanical performances and fracture mechanisms of boron-alloyed ferritic and martensitic stainless steels fabricated by powder metallurgy, Mater. Sci. Eng.-A **866**, 144680 (2023).
17 Y. Han, Z. H. Liu, C. B. Wu, Y. Zhao, G. Q. Zu, W. W. Zhu, and X. Ran, A short review on the role of alloying elements in duplex stainless steels, Tungsten **5**, 419 (2023).
18 H. Zhang, S. Hu, J. Shen, L. Ma, and F. Yin, Microstructures and mechanical properties of 30Cr-4Mo ferritic stainless steel joints produced by double-pulsed gas metal arc welding, Int. J. Adv. Manuf. Technol. **80**, 1975 (2015).
19 M. A. Khattak, S. Zaman, M. N. Tamin, S. Badshah, S. Mushtaq, and A. A. B. Omran, Effect of welding phenomenon on the microstructure and mechanical properties of ferritic stainless steel—A review, J. Adv. Res. Mater. Sci. **32**, 13 (2017).
20 Y. Geng, M. Akbari, A. Karimipour, A. Karimi, A. Soleimani, and M. Afrand, Effects of the laser parameters on the mechanical properties and microstructure of weld joint in dissimilar pulsed laser welding of AISI 304 and AISI 420, Infrared Phys. Tech. **103**, 103081 (2019).
21 L. M. Shen, Combined grain size, strain rate and loading condition effects on mechanical behavior of nanocrystalline Cu under high strain rates, Acta Mech. Sin. **28**, 1125 (2012).
22 X. Yang, H. Zhao, X. Gao, G. Lei, and Z. Chen, Molecular dynamics study on micro jet in single crystal aluminum, Acta Mech. Sin. **39**, 122232 (2023).
23 V. V. Pogorelko, and A. E. Mayer, Dynamic tensile fracture of iron: Molecular dynamics simulations and micromechanical model based

on dislocation plasticity, Int. J. Plast. **167**, 103678 (2023).
24 H. Ghaffarian, A. K. Taheri, K. Kang, and S. Ryu, Molecular dynamics simulation study on the effect of the loading direction on the deformation mechanism of pearlite, Multiscale Sci. Eng. **1**, 47 (2019).
25 Y. Cui, K. Song, Y. Bao, Y. Zhu, Q. Liu, and P. Qian, Effect of Cu and Mg co-segregation on the strength of the Al grain boundaries: A molecular dynamics simulation, Comput. Mater. Sci. **229**, 112391 (2023).
26 S. Plimpton, Fast parallel algorithms for short-range molecular dynamics, J. Comput. Phys. **117**, 1 (1995).
27 S. M. Eich, D. Beinke, and G. Schmitz, Embedded-atom potential for an accurate thermodynamic description of the iron-chromium system, Comput. Mater. Sci. **104**, 185 (2015).
28 M. Akhlaghi, T. Steiner, S. R. Meka, A. Leineweber, and E. J. Mittemeijer, Lattice-parameter change induced by accommodation of precipitate/matrix misfit; misfitting nitrides in ferrite, Acta Mater. **98**, 254 (2015).
29 N. N. Rammo, and O. G. Abdulah, A model for the prediction of lattice parameters of iron-carbon austenite and martensite, J. Alloys Compd. **420**, 117 (2006).
30 D. J. Evans, and B. L. Holian, The Nose-Hoover thermostat, J. Chem. Phys. **83**, 4069 (1985).
31 J. L. Shao, W. He, T. Xi, and J. Xin, Microscopic insight into the structural transition of single crystal iron under the ramp wave loading, Comput. Mater. Sci. **182**, 109772 (2020).
32 K. Wang, J. Chen, W. Zhu, W. Hu, and M. Xiang, Phase transition of iron-based single crystals under ramp compressions with extreme strain rates, Int. J. Plast. **96**, 56 (2017).
33 S. Rawat, and P. M. Raole, Molecular dynamics investigation of void evolution dynamics in single crystal iron at extreme strain rates, Comput. Mater. Sci. **154**, 393 (2018).
34 N. Y. Lopanitsyna, and A. Y. Kuksin, Nucleation and the spall strength of liquid metals, J. Phys.-Conf. Ser. **774**, 012030 (2016).
35 A. Stukowski, Visualization and analysis of atomistic simulation data with OVITO—the open visualization tool, Model. Simul. Mater. Sci. Eng. **18**, 015012 (2009).
36 D. Faken, and H. Jónsson, Systematic analysis of local atomic structure combined with 3D computer graphics, Comput. Mater. Sci. **2**, 279 (1994).
37 N. Saeidi, F. Ashrafizadeh, B. Niroumand, M. R. Forouzan, and F. Barlat, Damage mechanism and modeling of void nucleation process in a ferrite-martensite dual phase steel, Eng. Fract. Mech. **127**, 97 (2014).
38 H. Zhang, B. Wei, X. Ou, S. Ni, X. Liao, and M. Song, Enhancing $\{10\bar{1}2\}$ twin boundary migration capability in Ti-Al solid solution alloys with increasing Al content, J. Mater. Sci. Tech. **147**, 217 (2023).
39 D. Mukherjee, A. Forslund, L. Höglund, A. Ruban, H. Larsson, and J. Odqvist, Towards predictive simulations of spinodal decomposition in Fe-Cr alloys, Comput. Mater. Sci. **202**, 110955 (2022).
40 M. M. Asif , K. A. Shrikrishna, and P. Sathiya, Effects of post weld heat treatment on friction welded duplex stainless steel joints, J. Manuf. Process. **21**, 196 (2016).
41 B. Pricop, E. Mihalache, G. Stoian, F. Borza, B. Özkal, and L. G. Bujoreanu, Thermo-mechanical effects caused by martensite formation in powder metallurgy FeMnSiCrNi shape memory alloys, Powder Metallurgy **61**, 348 (2018).
42 C. Ji, X. Cai, Z. Zhou, F. Dong, S. Liu, and B. Gao, Effects of intermetallic compound layer thickness on the mechanical properties of silicon-copper interface, Mater. Des. **212**, 110251 (2021).
43 X. Zhou, W. Bu, S. Song, F. Sansoz, and X. Huang, Multiscale modeling of interfacial mechanical behaviours of SiC/Mg nanocomposites, Mater. Des. **182**, 108093 (2019).
44 D. Y. Sun, M. I. Mendelev, C. A. Becker, K. Kudin, T. Haxhimali, M. Asta, J. J. Hoyt, A. Karma, and D. J. Srolovitz, Crystal-melt interfacial free energies in hcp metals: A molecular dynamics study of Mg, Phys. Rev. B **73**, 024116 (2006).
45 A. Stukowski, and K. Albe, Dislocation detection algorithm for atomistic simulations, Model. Simul. Mater. Sci. Eng. **18**, 025016 (2010).
46 T. Suzuki, S. Takeuchi, and H. Yoshinaga, Dislocation Dynamics and Plasticity (Springer Science & Business Media, New York, 2013).
47 P. Franciosi, The concepts of latent hardening and strain hardening in metallic single crystals, Acta Metall. **33**, 1601 (1985).
48 D. D. Awale, V. D. Vijayanand, A. R. Ballal, M. M. Thawre, and G. V. Prasad Reddy, Study of microstructural transition in dissimilar weld joint from as-welded to PWHT condition using electron backscattered imaging, Mater. Lett. **285**, 129080 (2021).
49 W. Woo, V. T. Em, E. Y. Kim, S. H. Han, Y. S. Han, and S. H. Choi, Stress-strain relationship between ferrite and martensite in a dual-phase steel studied by in situ neutron diffraction and crystal plasticity theories, Acta Mater. **60**, 6972 (2012).

AISI 430不锈钢焊接接头的延伸率增强策略: 来自分子动力学分析的见解

卞功波, 刘锋, 张婷婷, 冉孟庭, 薛小炎, 武定泸, 王文先

摘要 AISI 430铁素体不锈钢在现代工业中应用广泛, 而传统的填充金属焊接方法得到的焊接接头具有抗拉强度(586 MPa)和延伸率(7.35%), 不足以满足日益增长的工程需求. 在这项工作中, 经过焊后热处理(PWHT)后, 接头的延伸率提高了一倍(15.11%), 而屈服强度保持不变. 热影响区(HAZ)的微观组织分析揭示了焊接接头在750 °C和800 °C下等轴铁素体、晶间马氏体和晶内针状马氏体之间的转变过程. 此外, 分子动力学模拟证明了不同类型马氏体在拉伸作用下对铁素体不锈钢单晶的影响. 结果表明, 晶间马氏体和针状马氏体表现为穿晶断裂, 而粒状马氏体表现为沿晶断裂. 晶间马氏体和粒状马氏体分布在晶体内部高应变区附近, 而针状马氏体则集中分布在晶界处, 远离高应变区. 不同类型马氏体硬化参数的比较表明, 粒状马氏体(58.98)比针状马氏体(97.40)和晶间马氏体(111.54)具有更高的塑性. 这些发现对于开发兼顾高延性和高强度的先进不锈钢焊接接头, 满足现代工程需求具有重要价值.